Hindawi

Research Article

Support Vector Regression Inverse System Control for Small Wind Turbine MPPT with Parameters' Robustness Improvement

Hongru Wang [1,2] **Zhigang Zhang** [1] **Wenjuan Zhang** [1] **Mengdi Li** [1] **and Yang Zhang** [2]

[1]*School of Electronic Information and Electrical Engineering, Changsha University, Changsha 410022, China*
[2]*School of Electronic Information and Electrical Engineering, Hunan University of Technology, Zhuzhou 412007, China*

Correspondence should be addressed to Wenjuan Zhang; 441291390@qq.com

With the increasing penetration of the permanent-magnet direct-drive wind power system, the maximum wind-energy capture and the generation speed control are more and more important. In the literature, the dynamic performance of the generator speed is well documented by the inverse system method. However, conventional inverse system methods have parameter dependency that is not sufficient to meet the dynamic requirements for permanent magnet synchronous generator (PMSG) speed tracking. Therefore, this paper introduces a support vector regression machine (SVR) method, especially for the inverse system model, which could solve the inaccurate parameters problems. As the SVR has the nonlinear approximation ability to identify and adjust the parameters online, thus, the system robustness could be improved. Finally, the dynamic performance of generator speed is evaluated by using the SVR method. Proposed theoretical developments are verified by the Simulink Test and experimental test.

1. Introduction

In the past decades, wind power is always the one of the fastest increasing renewable energy. The small wind turbine is widely used in industry due to its advantages characteristics such as low inertia, low design cost, and low requirements for construction sites [1]. Compared with traditional fixed speed WT systems, variable speed WT systems not only have the advantages of low production cost but also have advantages in increasing energy capture [2, 3].

The existing maximum wind-energy capture method, namely maximum power point tracking (MPPT) strategies for variable speed WT, can be classified into three methods: the optimal tip speed ratio control (TSR), the optimal torque control, and the perturbation observation method. Among the three methods, the TSR is the most widely used due to its quick response to the changing wind speed [4].

For the traditional TSR method, the linear controller is usually used to realize the decoupling control of PMSG. The design principle and structure of the linear controller are simple, but the linear regulation method is limited due to the controller linear nature [5, 6]. As PMSG is a nonlinear and strong coupling system, direct closed-loop control with a linear controller will lead to poor dynamic performance [7–9]. Under randomness and uncertainty of the wind speed condition, a faster and stable tracking of the rotor speed is necessary to ensure the maximum wind-energy capture efficiency [10, 11]. Considering that linear controllers such as proportional integral (PI), proportional derivative (PD), and proportional integral derivative (PID), they are more widely accepted in the industry [12, 13]. PMSG can be linearly compensated to make it more suitable for linear control law.

The inverse system method has been used for linear decoupling control such as applied for buck-converter control, which potentially improves the anti-interference performance with inverse system theory [14–16]. By constructing the inverse system and cascading the original system, the nonlinear original system has pseudolinear properties and is suitable for the linear control law [17]. Literature [18] establishes the mathematical model of the PMSG inverse system, and the pseudolinear system formed by cascading with the original system improves the dynamic

performance of the maximum wind-energy capture control. The mathematical model of PMSG is usually established in an ideal state. In actual working conditions, the inverse system model established by mathematical analysis is very sensitive to the parameters. When parameter perturbation occurs, the model needs to be reconstructed [19]. Recently, the machine learning method has been applied in various research fields, and it is used to imitate the learning ability of the human brain [20]. Literature [21] combined the machine learning method with the MPPT control of photovoltaic systems, which significantly improved the tracking speed and efficiency. Literature [22] applied the machine learning method to the wind power generation system to improve the system robustness in the case of wind speed fluctuations. Using machine learning methods, an inverse model can be obtained through a lot of training, which could improve wind-energy capture efficiency and avoid parameter perturbation problems.

The inverse model, based on machine learning and the neural network method, was used to the decoupling control of motor [23]. However, neural networks have black-box properties, and neural networks based on empirical risk minimization are easy to fall into local minimums and excessive reliance on experience, which reduces the use effect. Compared with neural networks, support vector machines (SVM) have the characteristics of small samples and high generalization ability. Literature [24] uses SVM instead of the neural network to establish an inverse system model when the accurate model of the motor is unknown, which effectively avoids problems such as overlearning and local minimization. Literature [25] uses the least square method to optimize the SVM algorithm and proposes an inverse system decoupling method based on LS-SVM. Using LS-SVM's ability to approximate and fit nonlinear functions, the model of the inverse system is obtained through training samples.

SVR, a learning machine based on the principle of statistical learning and structural risk minimization, introduces insensitivity coefficients ε on the basis of SVM, obtains a regression support vector machine, and achieves good performance [26, 27]. Compared with the neural network and least squares method and other empirical risk minimization methods, SVR can guarantee the global optimal solution and avoid the problem of getting into the local minimums [28]. Unfortunately, in previous studies, the inverse system and SVR methods were not used in PMSG to improve the efficiency of wind-energy capture.

In this paper, a maximum wind-energy capture control method based on the SVR inverse system (SIS) is proposed for PMSG WT. Two inverse models based on accurate analysis are designed. The SVR inverse model is used to replace the analytical model, and the two PID controllers are combined to achieve closed-loop decoupling control. The main contribution of this paper is to use the SVR method to train the analytical inverse system and obtain a model that does not depend on motor parameters so that the controller is robust to parameter perturbation and solve the model inaccuracy problem under various conditions. The Simulink and experiments results are provided to verify the conclusion of the theoretical study.

The remainder of this paper is organized as follows. The mathematical model of PMSG and problem analysis is presented in Section 2. The design process and control law, as well as the detailed analysis of the analytic inverse system and the SVR inverse system, are discussed in Section 3. The simulation results and experimental results are presented in Section 4. Section 5 concludes this paper.

2. Mathematical Modeling and Problem Analysis

The research object of this paper is a small wind power generation system. As shown in Figure 1, the wind turbine (WT) and PMSG are directly coupled and connected to DC-Link through a three-phase converter.

2.1. WT Model. The power obtained by wind turbine blades from wind energy can be expressed as follows:

$$P = 0.5\rho SV^3 Cp = 0.5\rho\pi R^2 V^3 Cp, \tag{1}$$

where ρ is the air density, S is the rotor swept area, V is the wind speed, R is the radius of the WT blade, and C_p is the power coefficient, which indicates the efficiency of WT to capture wind energy and estimated by

$$\begin{cases} Cp = 0.22\left(\dfrac{116}{\theta} - 0.4\beta - 5\right)e^{-(12.5/\theta)}, \\[4mm] \theta = \dfrac{1}{(1/\lambda + 0.08\beta) - \left(0.035/\beta^3 + 1\right)}, \end{cases} \tag{2}$$

where β is the pitch angle of the WT and λ is tip speed ratio, which is the ratio between the WT blade tip speed and the wind speed. TSR λ is given as follows:

$$\lambda = \frac{2\pi R\omega_0}{V} = \frac{\omega r R}{V}, \tag{3}$$

where ω_r (rad/s) is the rotor speed and ω_0 (r/min) is the rotational speed of the WT.

2.2. PMSG Model. In order to facilitate the analysis of the reversibility of the PMSG system, the mathematical model of PMSG's two-phase rotating coordinate is used as follows:

$$\begin{cases} u_d = R_s i_d + L_d \dfrac{\mathrm{d}i_d}{\mathrm{d}t} - \omega_r L_q i_q, \\[3mm] u_q = R_s i_q + L_q \dfrac{di_q}{dt} + \omega_r L_d i_d + \omega_r \psi_f, \\[3mm] T_e = \dfrac{3}{2}p_n \psi f i_q, \end{cases} \tag{4}$$

where R_s is the stator resistance; u_d and u_q are the stator voltages of the d-axis and q-axis, respectively; i_d and i_q are the stator currents of the d-axis and q-axis, respectively; L_d and L_q are the inductances of the d-axis and q-axis, respectively ($L_d = L_q = L$); ω_r is the rotor electrical speed; Ψ_f is
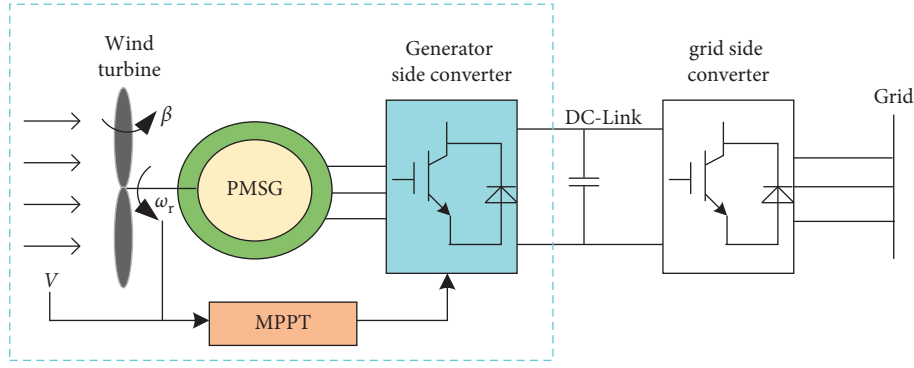
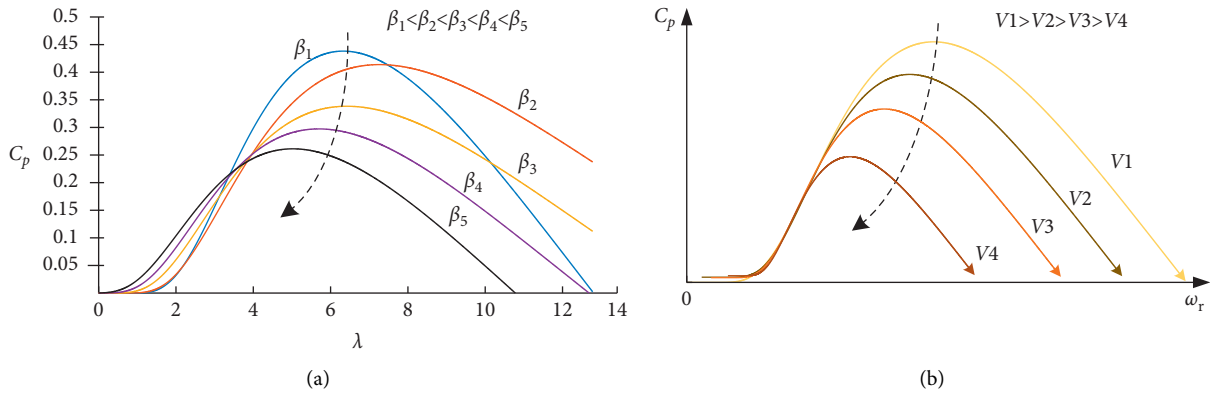FIGURE 1: PMSG wind power generator system structure.

(a)

(b)

FIGURE 2: (a) Relationship between C_p and λ and (b) relationship between C_p and ω_r.

the permanent-magnet flux; P_n is the number of pole pairs; J is the moment of inertia of the rotor; T_e is the electromagnetic torque; and TL is the load torque.

Therefore, the differential equation of PMSG in the two-phase rotating coordinate system can be expressed as follows:

$$
\begin{cases}
\dfrac{\mathrm{d}i_d}{\mathrm{d}t} = \dfrac{1}{L}u_d - \dfrac{R_s}{L}i_d + \omega_r i_q, \\[2mm]
\dfrac{di_q}{\mathrm{d}t} = \dfrac{1}{L}u_q - \dfrac{R_s}{L}i_q - \omega_r i_d - \dfrac{\omega_r \psi_f}{L}, \\[2mm]
\dfrac{\mathrm{d}\omega_r}{\mathrm{d}t} = \dfrac{3p_n^2 \psi_f i_q}{2J} - \dfrac{p_n T_L}{J}.
\end{cases}
\tag{5}
$$

2.3. Maximum Wind-Energy Capture for Wind Turbines. The maximum wind-energy capture control occurs in the variable power stage of the wind power generation system when the wind speed is lower than the rated wind speed. The power coefficient C_p can be obtained by (2) and (3), as shown in Figure 2.

Figure 2 shows the relationship between the β, λ, and C_p. When fixed at an optimal value, there is an optimal tip speed ratio to keep the C_p at the maximum value, which provides a

theoretical basis for the maximum wind-energy capture of the wind power generation system. The control goal of this paper is to maximize the C_p of the WT by controlling the speed of PMSG. This method sets the optimal tip speed ratio value as the reference speed. Moreover, the traditional TSR usually uses vector decoupling control based on PI, which will lead to poor dynamic performance.

3. Design of the SVR Inverse System Model

3.1. Analytic Inverse System of the PMSG. PMSG original system (hereafter, it is referred to as the original system) is considered a nonlinear system with two inputs and two outputs. The next step is to analyze the reversibility of the original system. $u = [u_d, u_q]^T$, $x = [i_d, i_q, \omega_r]^T$, and $y = [i_d, \omega_r]^T$ were set as the input, state, and output variables, respectively, as presented by

$$
\begin{cases}
u = [u_1, u_2]^T = [u_d, u_q]^T, \\
x = [x_1, x_2, x_3]^T = [i_d, i_q, \omega_r]^T, \\
y = [y_1, y_2]^T = [i_d, \omega_r]^T.
\end{cases}
\tag{6}
$$

The following equation represents the original system state equation of PMSG:

$$
\begin{cases}
\dot{x}_1 = \dfrac{1}{L}u_1 - \dfrac{R_s}{L}x_1 + x_2 x_3, \\[2ex]
\dot{x}_2 = \dfrac{1}{L}u_2 - \dfrac{R_s}{L}x_2 - x_1 x_2 - \dfrac{\psi_f}{L}x_3, \\[2ex]
\dot{x}_3 = \dfrac{3p_n^2 \psi_f}{2J}x_2 - \dfrac{p_n T_L}{J}.
\end{cases}
\tag{7}
$$

The output equation of the original system is given by

$$
y = [y_1, y_2]^T = [i_d, \omega_r]^T = [x_1, x_3]^T.
\tag{8}
$$

Adopting the theory of inverse system and interactor, the output y is differentiated until u occurs in the result, as shown in

$$
\begin{cases}
y_1' = \dfrac{1}{L}u_1 - \dfrac{R}{L}x_1 + x_2 x_3, \\[2ex]
y_2'' = \dfrac{3p_n^2 \psi_f}{2J}\left(\dfrac{1}{L}u_2 - \dfrac{R}{L}x_2 - x_1 x_3 - \dfrac{\psi_f}{L}x_3\right).
\end{cases}
\tag{9}
$$

To achieve $Y_1 = y_1'$ and $Y_2 = [y_1', y_2'']^T$, the Jacobin matrix can be obtained as shown in

$$
\begin{cases}
\dfrac{\partial Y_1}{\partial u} = \left[\dfrac{\partial \dot{y}_1}{\partial u_1}, \dfrac{\partial \dot{y}_1}{\partial u_2}\right] = \left[\dfrac{1}{L}, 0\right], \\[3ex]
\dfrac{\partial Y_2}{\partial u^T} = \begin{bmatrix} \dfrac{\partial \dot{y}_1}{\partial u_1} & \dfrac{\partial \dot{y}_1}{\partial u_2} \\[1.5ex] & \dfrac{\partial \ddot{y}_2}{\partial u_2} \\[1.5ex] \dfrac{\partial \ddot{y}_2}{\partial u_2} & \end{bmatrix} = \begin{bmatrix} \dfrac{1}{L} & 0 \\[2ex] 0 & \dfrac{3p_n^2 \psi_f}{2LJ} \end{bmatrix}.
\end{cases}
\tag{10}
$$

The full rank of the two Jacobian matrices in (10) is given in

$$
\begin{cases}
\alpha_1 = \mathrm{rank}\left[\dfrac{\partial Y_1}{\partial u}\right] = 1, \\[3ex]
\alpha_2 = \mathrm{rank}\left[\dfrac{\partial Y_2}{\partial u^T}\right] = 2.
\end{cases}
\tag{11}
$$

The relative order of the vector can be obtained according to (11): $\alpha = [\alpha_1, \alpha_2]^T = [1, 2]^T$ and $\alpha_1 + \alpha_1 = 1 + 2 \le n = 3$, where n is the order of the original system of PMSG. This proves the reversibility of the original PMSG system. $v = [v_1, v_2]^T = [y_1', y_2'']^T = [i_d', \omega_r'']^T$ was selected as the input variable of the inverse system; $u = [u_1, u_2]^T = [u_d, u_q]^T$, which is the output variable of the inverse system; and T_L is the load torque, and its value is obtained from the PMSG original system observation. When these are combined with (9), the inverse system can be expressed by

$$
\begin{cases}
u_1 = Lv_1 + Rx_1 - Lx_2 x_3, \\[2ex]
u_2 = \dfrac{2JL}{3p_n^2 \psi_f}v_2 + Rx_2 + Lx_1 x_3 + \psi_f x_3.
\end{cases}
\tag{12}
$$

Equation (12) can be rewritten as follows:

$$
\begin{cases}
u_d = Li_d' + Ri_d + \dfrac{2LJ\omega_r}{3p_n^2 \psi_f}\left(\omega_r' + \dfrac{p_n T_L}{J}\right), \\[3ex]
u_q = \psi_f \omega_r + Li_d \omega_r + \dfrac{2LJ\omega_r''}{3p_n^2 \psi_f} + \dfrac{2RJ\omega_r'}{3p_n^2 \psi_f} + \dfrac{2RT_L}{3p_n \psi_f}.
\end{cases}
\tag{13}
$$

Equation (13) is the inverse-system analytical expression based on the PMSG mathematical model. The inverse system consists of two inputs (i_d, ω_r) and two outputs (u_d, u_q).

The PMSG is dynamically decoupled into a first-order linear current subsystem and a second-order linear speed subsystem through the inverse system method. The pseudolinear system constructed by cascading the two systems is shown in Figure 3.

3.2. Inverse System Modeling of SVR.

The training sample of the inverse model is set to $T = \{(x_i, y_i), \ i = 1, \ldots, l\} \subset R^N \times R$, where x_i is the input sample containing six features ($i_d, i_d', \omega, \omega', \omega'', T_L$), and the two features u_d and u_q are contained in the output sample y_i. The function model determined by the SVR method can be regarded as a hyperplane in the kernel space, as follows:

$$
f(x) = (w, \varphi(x)) + b, \ (\varphi: R^N \longrightarrow F, w \in F),
\tag{14}
$$

where w is the weight vector of hyperplane $f(x)$, b is a bias term, and $\varphi(x)$ means to map data R^N to a high-dimensional feature space F.

The optimization problems of the SVR are expressed as follows:

$$
\min_{w, \xi, \xi^*} = \dfrac{1}{2}\|w\|^2 + C\sum_{i=1}^{l}(\xi_i + \xi_i^*),
\tag{15}
$$

where $(1/2)\|w\|^2$ is the minimized structural risk and the $C\sum_{i=1}^{l}(\xi_i, \xi_i^*)$ is the minimized sample error. Two nonnegative variables ξ_i and ξ_i^* are used to weaken the constraints of some sample points. The positive number C is a compromise between structural risk and sample error.

The constraint conditions are expressed as follows:

$$
\begin{cases}
y_i - f(x_i) \le \varepsilon + \xi_i, \\
f(x_i) - y_i \le \varepsilon + \xi_i^*, \\
\xi_i, \xi_i^* \ge 0,
\end{cases}
\tag{16}
$$

where ε is the introduced insensitive coefficient to avoid overfitting. In order to solve (15), Lagrange multipliers $\alpha_i, a_i^* \ge 0$ and $\eta_i, \eta_i^* \ge 0$ are introduced. Reconstruct the above optimization problem as a Lagrangian function, as follows:
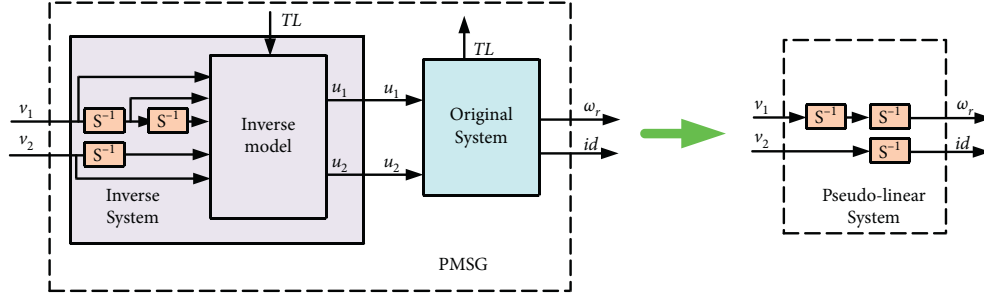
FIGURE 3: Diagram of pseudolinear system.

$$L = \frac{1}{2}\|w\|^2 + C\sum_{i=1}^{l}(\xi_i + \xi_i^*) - \sum_{i=1}^{l}(\xi_i\eta_i + \xi_i^*\eta_i^*)$$

$$- \sum_{i=1}^{l}\alpha_i[\xi_i + \varepsilon + y_i - (w, \phi(x)) - b] \qquad (17)$$

$$- \sum_{i=1}^{l}\alpha_i^*[\xi_i + \varepsilon - y_i + (w, \phi(x)) + b].$$

Introduce a kernel function that satisfies the Mercer condition to replace the inner product of the high-dimensional kernel space in the (17); here, the Gaussian kernel is used. The kernel function can be written as follows:

$$K(x_i, x_j) = \exp\left[-\gamma\left(\sum_{k=1}^{n}(x_{ik} - x_{jk})^2\right)\right]. \qquad (18)$$

The optimized problem can be expressed as follows:

$$\min_{\alpha,\alpha^*} = \frac{1}{2}\sum_{i=1,j=1}^{l}(\alpha_i - \alpha_i^*)(\alpha_j - \alpha_j^*)K(x_i, x_j)$$

$$+ \varepsilon\sum_{i=1}^{l}(\alpha_i + \alpha_i^*) - \sum_{i=1}^{l}(\alpha_i - \alpha_i^*)y_i, \qquad (19)$$

and the constraint conditions are expressed as follows:

$$\left\{\sum_{i=1}^{l}(\alpha_i - \alpha_i^*) = 0, \quad \alpha_i \geq 0, \alpha_i^* \leq C. \qquad (20)\right.$$

In the solution of (22), part of the coefficient $(\alpha_i - a_i^*)$ is not zero. The sample (x_i, y_i) corresponding to nonzero $(\alpha_i - a_i^*)$ is the support vector. The optimized (14) is expressed as follows:

$$f(x) = \sum_{i=1}^{l}(\overline{\alpha}_i^* - \overline{\alpha}_i)K(x_i, x) + \overline{b}. \qquad (21)$$

Therefore, the inverse model based on SVR can be expressed as follows (Figure 4):

$$\left\{\begin{array}{l} f_q(x) = \sum_{i=1}^{l}(\overline{\alpha}_{qi}^* - \overline{\alpha}_{qi})K(x_i^q, x) + \overline{b}_q, \\[3mm] f_d(x) = \sum_{i=1}^{l}(\overline{\alpha}_{di}^* - \overline{\alpha}_{di})K(x_i^d, x) + \overline{b}_d. \end{array}\right. \qquad (22)$$
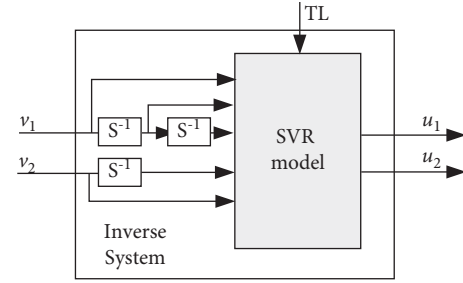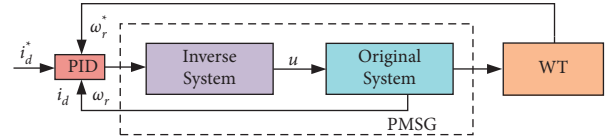

FIGURE 4: Inverse system modeling of SVR.

FIGURE 5: Control block diagram of the maximum wind-energy capture controller based on the inverse system.

As shown in Figure 4, the SVR model is used instead of the analytical model. The SVR inverse system model gets rid of the dependence on the precise mathematical model of the control object.

3.3. A Control Strategy Based on SVR Inverse System Decoupling for Maximum Wind-Energy Capturing.

To maximize the wind-energy capture, a vector control strategy of $id = 0$ is adopted in combination with the PMSG speed control based on the PI vector control and inverse system (Figure 4). The real-time wind speed of the WT is measured, and the reference speed is calculated according to (3) to maintain the WT running at the optimal blade-TSR. The reference speed is used as the input of the controller speed outer loop. The inner loop is the current loop and is set to 0. Figure 5 shows the equivalent control block diagram of the MWECIS.

Figure 6 shows the PMSG control block diagram based on the SVR inverse system decoupling. In Figure 6, the inverse system is merged with the original system to form a pseudolinear system. Therefore, the system will adapt to the linear control law. A PID control can achieve the good dynamic decoupling effect so that the speed of PMSG can
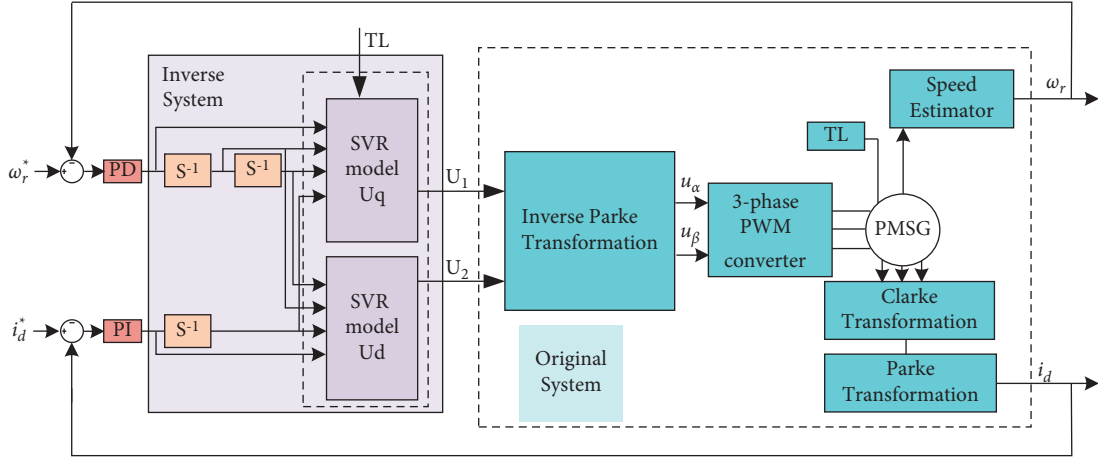
FIGURE 6: Control block diagram of the PMSG based on the SIS method.

promptly follow the change in the wind speed and keep the WT always running at the optimal blade-TSR.

4. Decoupling Control of PMSG Based on SVR Inverse System

4.1. Simulation Results. In order to verify the effectiveness of the proposed SIS method, the SIS is compared with the analytical inverse system method (AIS) and the traditional TSR method. The AIS method will be designed as two controllers. For the AIS-I type controller, the parameters in the mathematical model are completely matched with the actual parameters of the motor. For the AIS-II controller, there is a 30% error between the parameters in the mathematical model and the actual parameters of the motor.

The parameters of the SIS, TSR, AIS-I, and AIS-II were well tuned through trial and error. The parameters of PMSG and WT are shown in Table 1.

4.1.1. Simulation of AIS-I, TSR, and SIS Controllers. In order to reflect the improvement of the dynamic performance of the control system by the inverse system method, the selected wind speed is shown in Figure 7.

It can be seen from Figure 7 that the wind speed fluctuates randomly between 2 m/s and 8 m/s. Figure 7 is used as the input wind speed, and the speed response of the generator is shown in Figure 8.

As shown in Figure 8(a), the PMSG rotor speed based on the AIS-I controller can quickly and stably follow the reference speed. As shown in Figure 8(b), the PMSG rotor speed based on the TSR controller produces a large overshoot when the reference speed is abruptly changed. For example, at 1.5 s, the speed response of PMSG is 150 r/min, while the reference speed is 200 r/min. As shown in Figure 8(c), the controller based on the SIS method almost perfectly approximates the AIS-I controller, and the PMSG rotor speed can quickly and stably follow the reference speed. The error between the speed response and the reference speed of the PMSG is shown in Figure 9.

TABLE 1: Key simulation parameters of PMSG and WT.

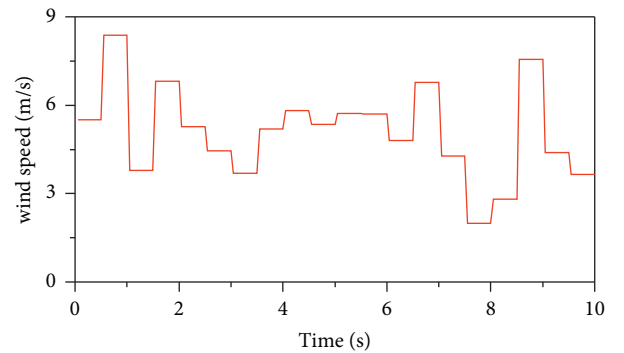| Parameter	Value	Units
R_s	0.6	Ω
L	0.002	H
J	0.0086	$kg \cdot m^2$
P	8	poles
ψ_f	0.35	Wb
R	1.5	m
β	0	
λ_{opt}	8.1	

FIGURE 7: Wind speed.

It can be seen from Figure 9 that the controller based on the SIS method has the same rotational speed error as the controller based on the AIS-I method. At 3.5 s–3.6 s, the PMSG rotational speed error of the TSR method is twice that of the SIS method and the AIS-I method. The tip speed ratio λ of the three control methods is shown in Figure 10.

As shown in Figure 10, the optimum tip speed ratio λ_{opt} for the wind turbine is 8.1. In 1.2 s–1.4 s, the λ of the TSR method fluctuated around 8.1, while the λ of the SIS and AIS-I methods remained at 8.1. The power coefficient C_p of the WT is shown in Figure 11.

It can be seen from Figure 11 that the power coefficient C_p of WT under different methods and the maximum of C_p
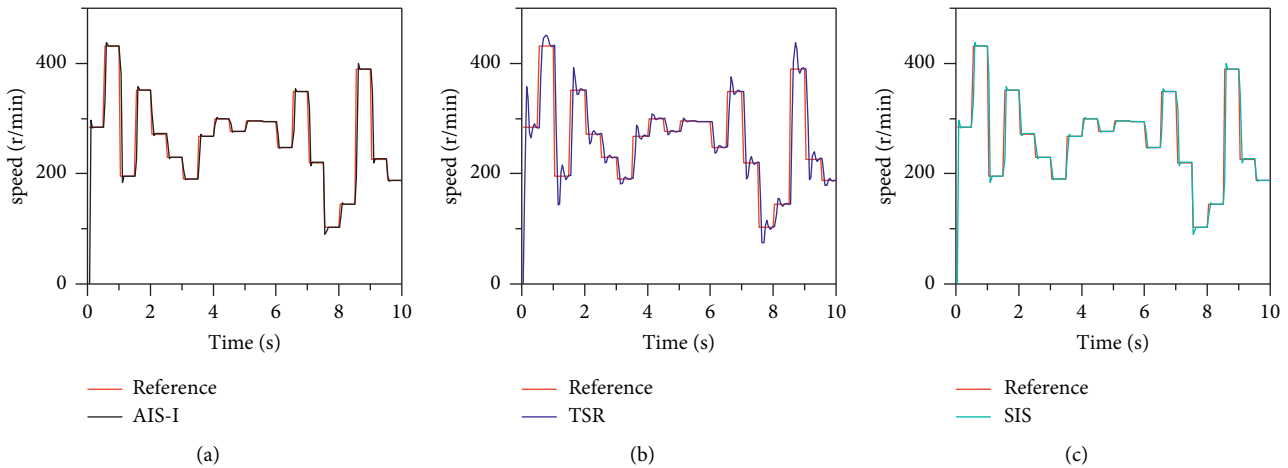
FIGURE 8: Simulated speed response: (a) speed response based on the AIS-I method, (b) speed response based on the TSR method, and (c) speed response based on the SIS method.
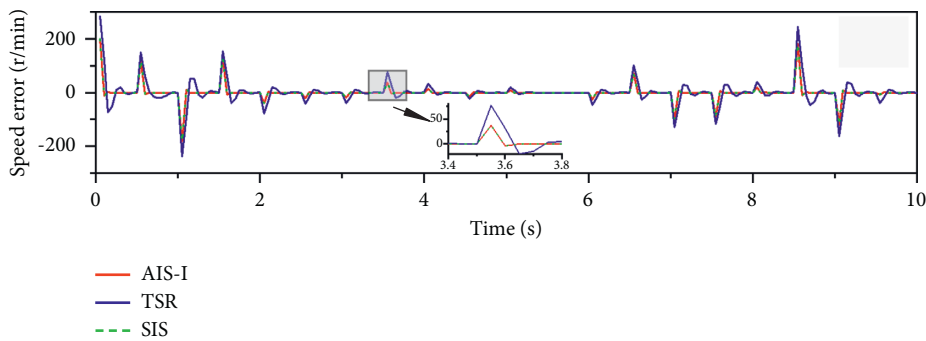

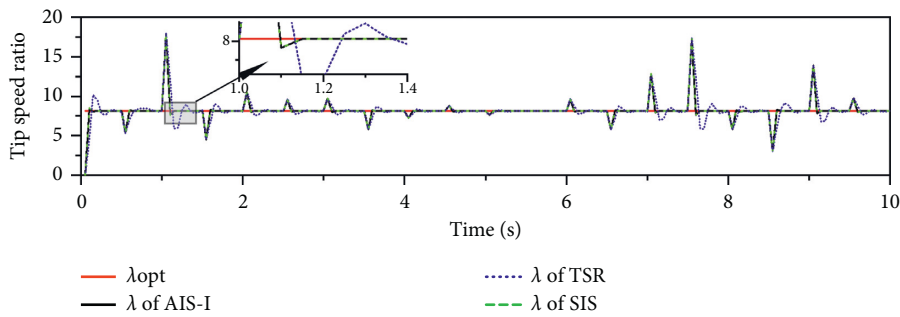FIGURE 9: Simulated error between speed response and reference speed.

FIGURE 10: Tip speed ratio based on AIS-I, TSR, and SIS methods.

is 4.8. As shown in Figure 11(a), the AIS-I method can keep the WT in the state of maximum wind-energy capture. When the wind speed changes suddenly, the C_p drops briefly and then returns to 4.8. As shown in Figure 11(b), compared with ASI-I, the average C_p of the TSR method is lower. When the wind speed changes, the C_p adjustment time based on the TSR method is longer. As shown in Figure 11(c), the C_p based on the SIS method can well approximate the C_p of the AIS-I method. The output power (Pm) response based on different methods is presented in Figure 12.

As shown in Figure 12, it is the output power of the wind turbine. For the same wind speed input, the wind turbine output power of AIS-I and SIS methods is higher than that of the TSR method.

Compared with the traditional TSR method, both AIS-I and SIS methods can make PMSG obtain better dynamic performance. The faster and more stable control of PMSG rotor speed enables wind turbines to maintain high efficiency and capture more wind energy. The proposed SIS method can well approximate the AIS-I method and achieve the same control effect.
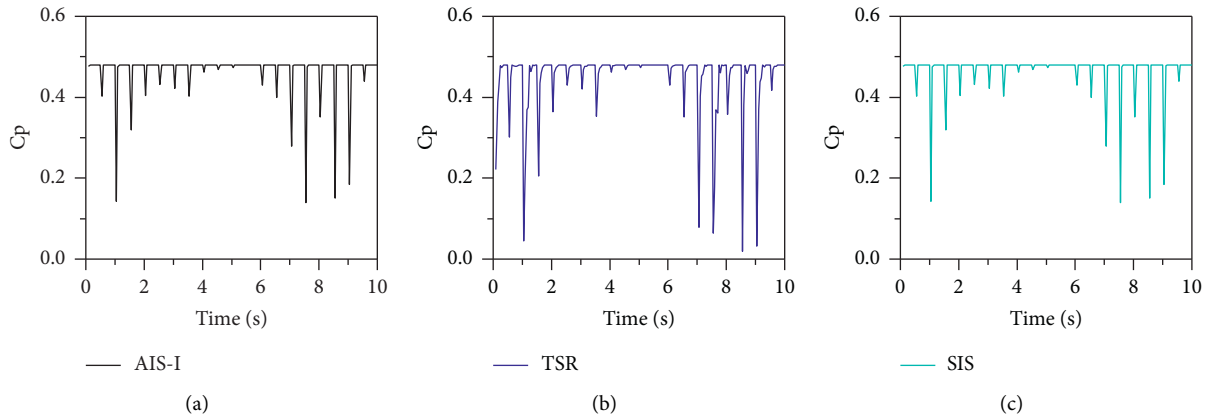
FIGURE 11: Power coefficient C_p of the wind turbine: (a) C_p based on the AIS-I method, (b) C_p based on the TSR method, and (c) C_p based on the SVR method.
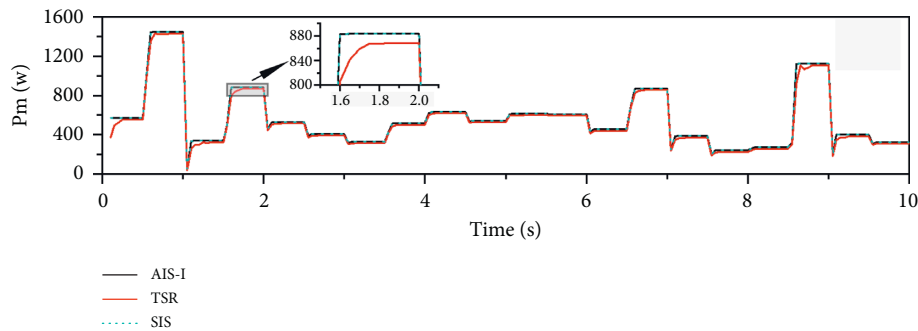

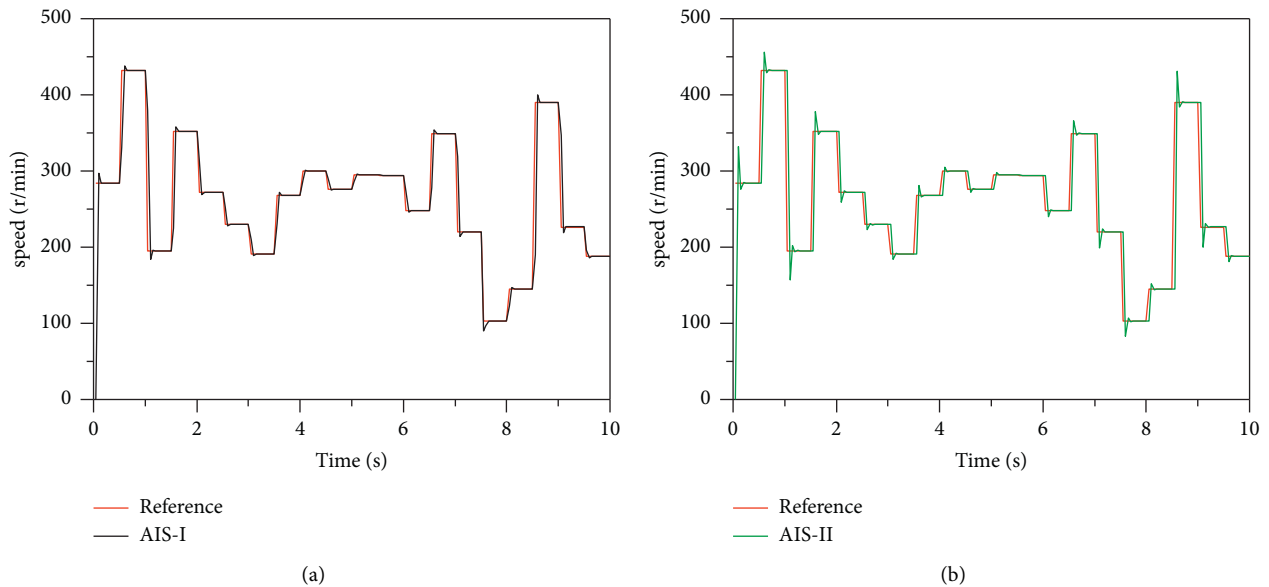FIGURE 12: The output power response based on different methods.

FIGURE 13: Simulated speed response: (a) speed response based on the AIS-I method and (b) speed response based on AIS-II method.

4.1.2. Simulation of AIS-I and AIS-II Controllers. The analytical inverse system method is designed as two controllers to study the influence of inaccurate PMSG parameters on the control effect. The input wind speed is shown in Figure 7,

and the speed responses of the two controllers are shown in Figure 13.

As can be seen from Figure 13, it is the rotational speed response of the PMSG. As shown in Figure 13(a), the speed
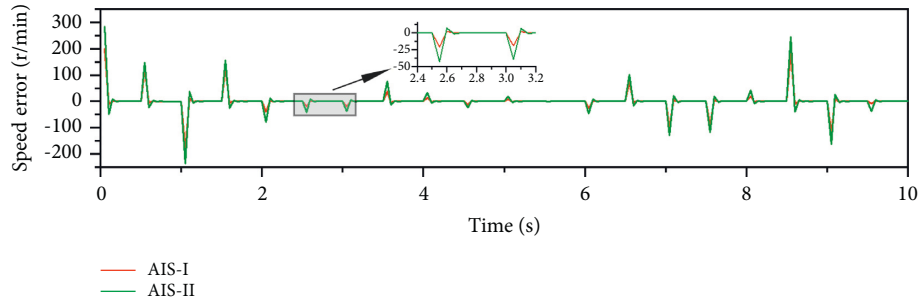
FIGURE 14: Simulated error between speed response and reference speed.
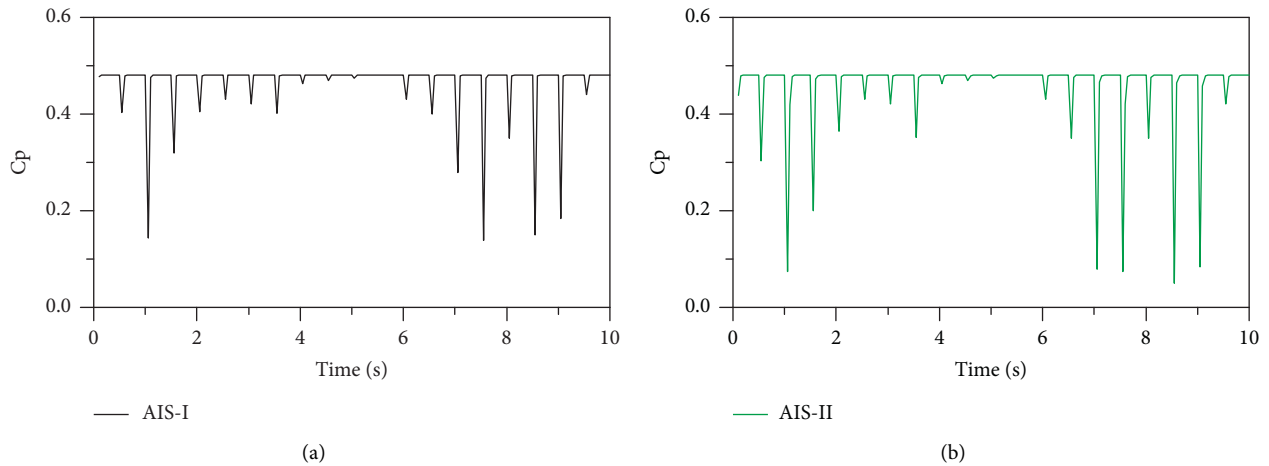

(a)

(b)

FIGURE 15: Power coefficient C_p of the wind turbine: (a) C_p based on the AIS-I method and (b) C_p based on the AIS-II method.
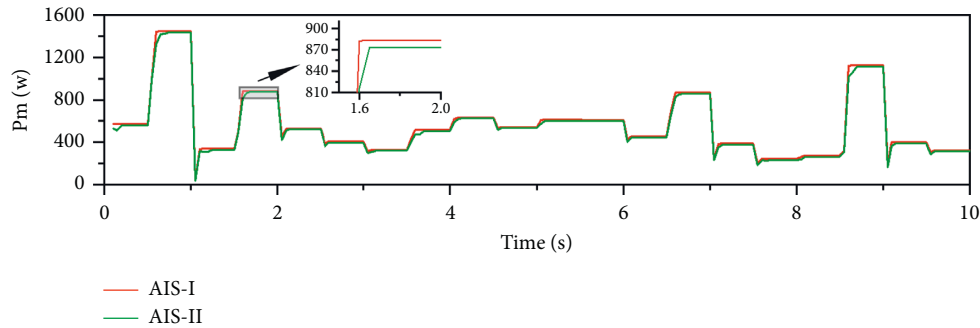

FIGURE 16: The output power response based on AIS-I and AIS-II methods.

response based on the AIS-I method can follow the reference speed quickly and stably, and the overshoot and adjustment time are very small. As shown in Figure 13(b), compared with AIS-1, the speed response based on the AIS-2 method will have a larger overshoot when the wind speed is abruptly changed. The error between the speed response and the reference speed of the PMSG is shown in Figure 14.

Figure 14 shows the rotational speed error of two different methods. Between 2.4 s and 3.2 s, the rotational speed error of the AIS-2 method is twice that of the AIS-1 method. The power coefficient C_p of the WT is shown in Figure 15.

It can be seen from Figure 15 that the power coefficient C_p of WT under different methods and the maximum of C_p is 4.8. As shown in Figure 11(a), the AIS-1 method can keep

the WT in the state of maximum wind-energy capture. When the wind speed changes suddenly, the C_p drops briefly and then returns to 4.8. As shown in Figure 11(b), compared with AIS-1, the C_p adjustment time based on the AIS-2 method is longer when the wind speed changes. The output power (Pm) response based on different methods is presented in Figure 16.

As shown in Figure 16, it is the output power of the wind turbine. For the same wind speed input, the wind turbine output power of AIS-1 is higher than that of the AIS-2 method.

From the simulation results, the method of AIS has better dynamic performance than the TSR method, which enables the WT to capture more wind energy. However,
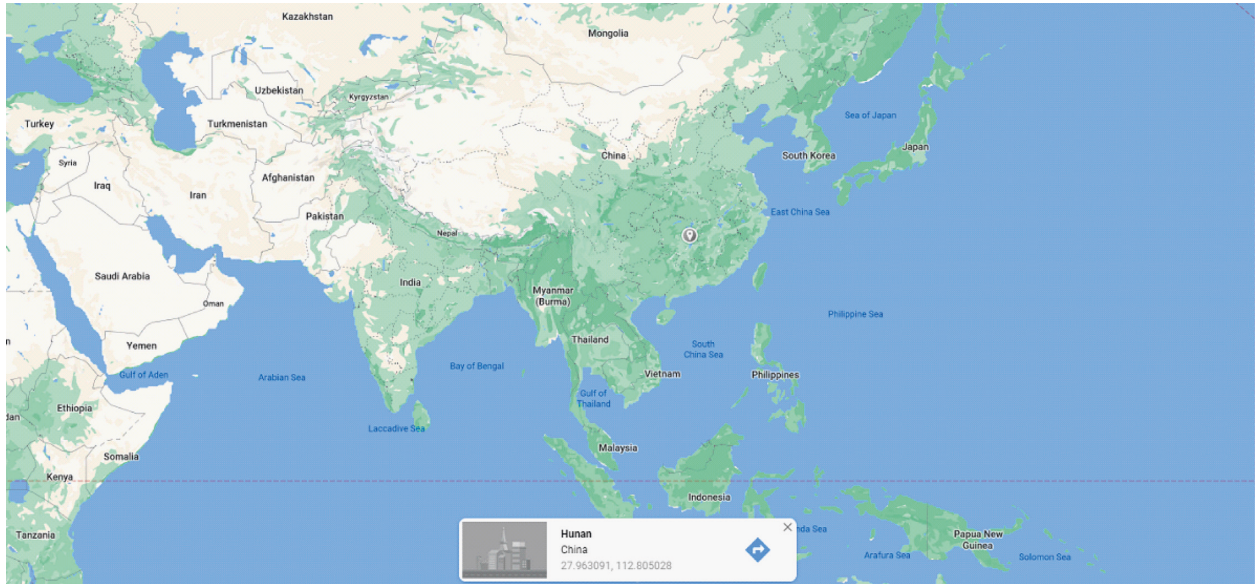
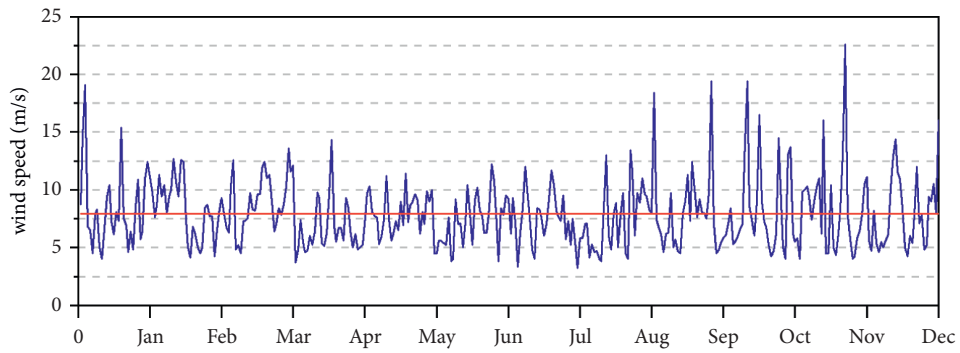Figure 17: Location of the studied site.

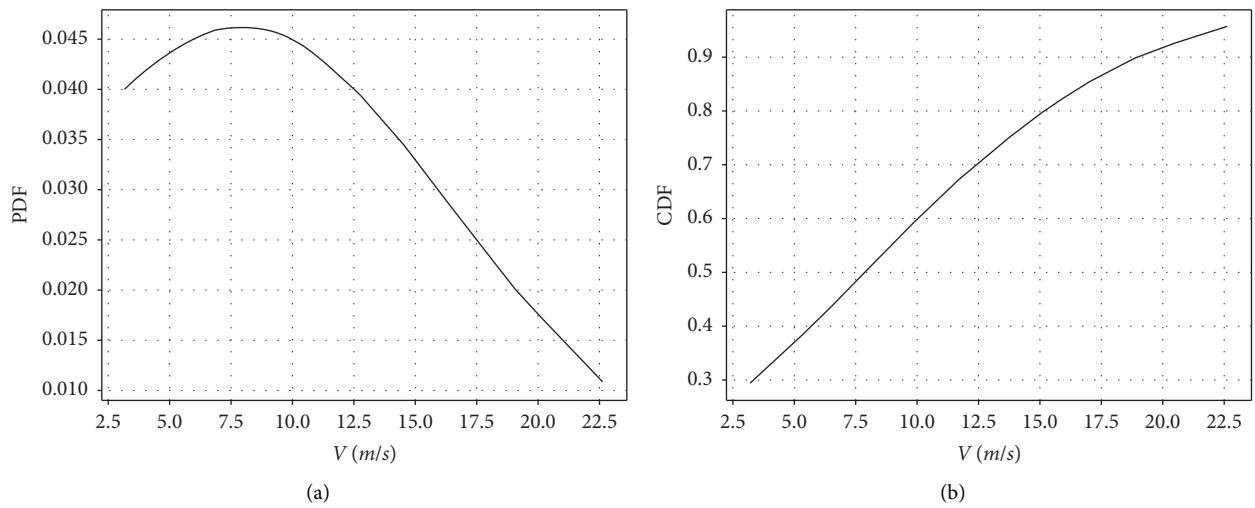Figure 18: Wind speed data at Hunan in 2020.

(a)

(b)

Figure 19: (a) Rayleigh probability distributions function PDF and (b) Rayleigh cumulative distributions function CDF.
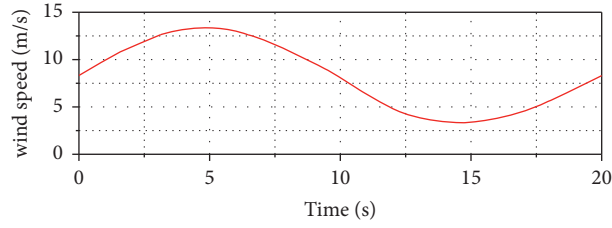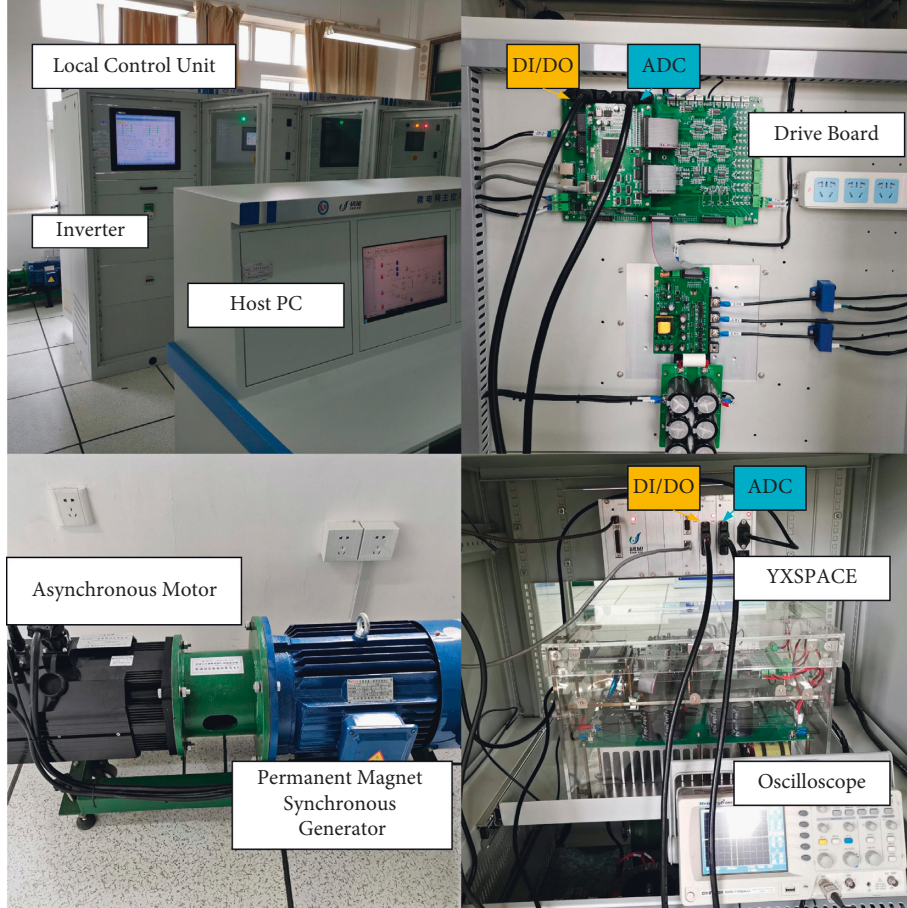
FIGURE 20: Wind speed profile.

FIGURE 21: Experiment platform.

when the parameters of the PMSG are imprecise, the control effect of the AIS method becomes poor. The proposed SIS method can approximate the AIS method, avoid the problem of inaccurate parameters, and improve the dynamic performance and robustness of the system.

4.2. Experiment Results. In order to ensure that the experimental data are closer to the actual working conditions, we obtained the 2020 annual wind speed data from NASA Power data [29] in Hunan Province, China (where the laboratory is located, Figure 17), as shown in Figure 18.

As shown in Figure 8, the wind speed in Hunan in 2020 varies from 3 m/s to 22.5 m/s, and the average wind speed is

TABLE 2: Key parameters of PMSG and WT.

Parameter	Value	Units
R_s	0.62	Ω
L	0.002	H
J	0.0086	kg $\cdot$ m^2
P	8	#Poles
ψ_f	0.35	Wb
R	2	m
β	0	
λ_{opt}	8.1	

7.9 m/s. Using Python, combined with Rayleigh law [30] to analyze wind speed data, Rayleigh law mainly depends on the average value of wind speed.
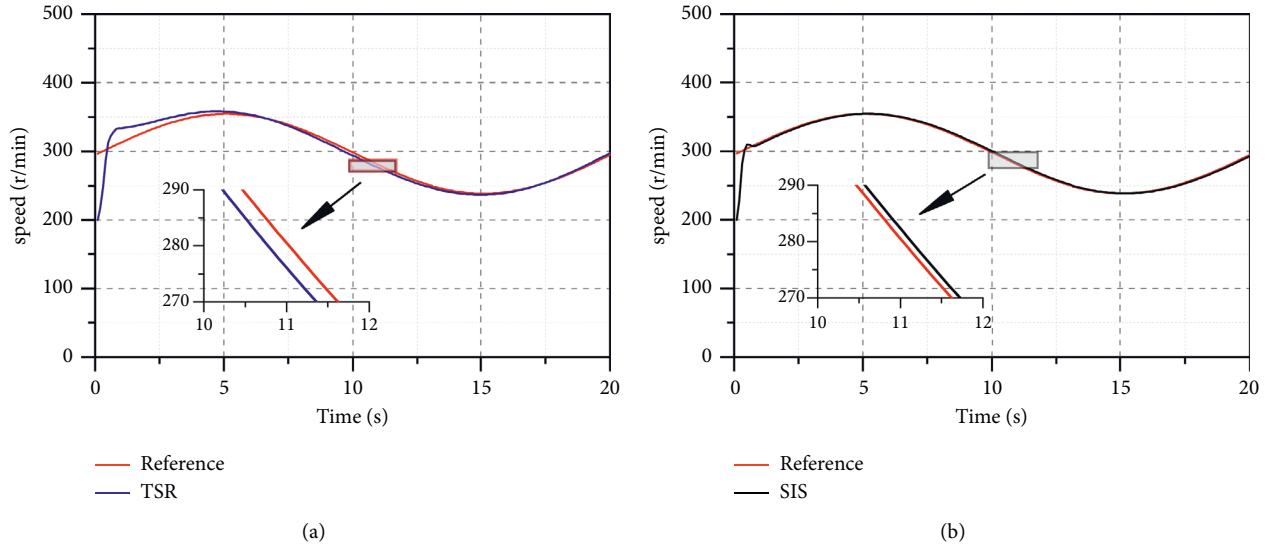
FIGURE 22: Experimental speed response: (a) speed response based on TSR method and (b) speed response based on the SIS method.

The probability density function (PDF) is expressed as follows:

$$f(V) = \frac{\pi}{2} \frac{V}{\overline{V}} \exp\left(-\left[\frac{\pi}{4}\left(\frac{V}{\overline{V}}\right)^2\right]\right). \tag{23}$$

The cumulative distribution function (CDF) is expressed as follows:

$$P(V) = 1 - \exp\left(-\left[\frac{\pi}{4}\left(\frac{V}{\overline{V}}\right)^2\right]\right). \tag{24}$$

Figure 19 shows the output PDF and CDF after Rayleigh distribution processing on wind speed data.

As shown in Figure 19, the Rayleigh probability density function PDF is basically consistent with the measured wind speed data. Most wind speeds throughout the year are concentrated between 2.5 and 12.5 m/s, and the cumulative distribution function CDF also grows fastest in this interval. Therefore, we can determine the validity of the Rayleigh distribution and classify it as a normal distribution.

The analysis of wind speed data is applied to simulation and experiment, simulate similar curve distribution, meet 2.5–12.5 m/s variable wind speed, and provide corresponding aerodynamic torque to drive PMSG with an interval of 20 s.

As shown in Figure 20, it is a 20 s wind speed graph, and the change law conforms to the above-mentioned wind speed data analysis. The wind speed in Figure 20 will be used in experiments.

The experimental platform is shown in Figure 21, which includes the asynchronous motor and PMSG. The wind turbine is simulated by an asynchronous motor, which drives by a 7.5 kW ABB inverter. The experiment programming is completed by the YXSPACE rapid prototyping controller.

The key parameters of PMSG and WT in the experiment are listed in Table 2.

The input wind speed is shown in Figure 20; the experiment time is 30 s; and the result is shown in Figure 22.

Figure 22(a) shows the reference speed and response speed with the TSR method. It could be seen that the overshoot in the start-up phase is 10%, and the adjustment time is 3 s. When the wind speed is changed, the rotor speed differs from the reference speed by 5 r/min. Figure 22(b) shows the reference speed and response speed with the SIS method. It could be seen that a small speed overshoot in the start-up phase. During the wind speed change phase, the two curves basically coincide. When using the SIS method, the rotor speed can quickly and stably follow the reference speed.

5. Conclusions

In this study, the proposed SIS method can successfully approach the analytical inverse system. The SVR model could successfully transfer the nonlinear PMSG speed control system into a pseudolinear system with linear properties. Using the maximum wind-energy capture control, SIS can avoid the parameter perturbation problem faced by the analytical inverse system method and has more stable performance under actual working conditions. Simulation and experimental results show that the proposed SIS control strategy provides stable and fast control effects for the rotor speed of PMSG and can achieve greater wind-energy capture under simulated real wind speed. Finally, the research in this paper focuses on using the SIS method to control WT to capture more wind energy, and the work of transferring energy into the grid is done by grid-side inverters. Therefore, it is strongly recommended to apply the SIS method to the grid-side inverter control in future work. The PMSG system

will better control the transmission of active power and reactive power to the grid.

Data Availability

The data used to support the findings of this study are included within the article.

Conflicts of Interest

The authors declare that there are no conflicts of interest regarding the publication of this paper.

Acknowledgments

References

[1] R. Veena, V. Femin, S. Mathew, I. Petra, and J. Hazra, "Intelligent models for the power curves of small wind turbines," in *Proceedings of the 2016 International Conference on Cogeneration, Small Power Plants and District Energy (ICUE)*, pp. 1–5, Bangkok, Thailand, September 2016.

[2] L. Y. Wang, L. X. Cao, and L. Zhao, "Non-linear tip speed ratio cascade control for variable speed high power wind turbines: a backstepping approach," *IET Renewable Power Generation*, vol. 12, no. 8, pp. 968–972, 2018.

[3] K. Yenduri and P. Sensarma, "Maximum power point tracking of variable speed wind turbines with flexible shaft," *IEEE Transactions on Sustainable Energy*, vol. 7, no. 3, pp. 956–965, 2016.

[4] M. Nasiri, J. Milimonfared, and S. H. Fathi, "Modeling, analysis and comparison of TSR and OTC methods for MPPT and power smoothing in permanent magnet synchronous generator-based wind turbines," *Energy Conversion and Management*, vol. 86, pp. 892–900, 2014.

[5] D. Zouheyr, B. Lotfi, and B. Abdelmadjid, "Improved hardware implementation of a TSR based MPPT algorithm for a low cost connected wind turbine emulator under unbalanced wind speeds," *Energy*, vol. 232, Article ID 121039, 2021.

[6] K. K. Prabhakaran and R. Saravanakumar, "Maximum power extraction from a wind turbine using terminal synergetic control," *IETE Journal of Research*, vol. 8, pp. 1–8, 2020.

[7] Z. Y. Chen, M. H. Yin, L. J. Zhou, Y. P. Xia, J. K. Liu, and Y. Zou, "Variable parameter nonlinear control for maximum power point tracking considering mitigation of drive-train load," *Ieee-Caa Journal of Automatica Sinica*, vol. 4, no. 2, pp. 252–259, 2017.

[8] B. Boukhezzar and H. Siguerdidjane, "Nonlinear control of a variable-speed wind turbine using a two-mass model," *IEEE Transactions on Energy Conversion*, vol. 26, no. 1, pp. 149–162, 2011.

[9] S. Rajendran and D. Jena, "Variable speed wind turbine for maximum power capture using adaptive fuzzy integral sliding mode control," *Journal of Modern Power Systems and Clean Energy*, vol. 2, no. 2, pp. 114–125, 2014.

[10] H. Geng and G. Yang, "Linear and nonlinear schemes applied to pitch control of wind turbines," *The Scientific World Journal*, vol. 2014, Article ID 406382, 9 pages, 2014.

[11] S. AlSabbah, M. AlDhaifallah, and A. Al-Jarrah, "Design of multiregional supervisory fuzzy PID control of pH reactors," *Journal of Control Science and Engineering*, vol. 2015, Article ID 396879, 9 pages, 2015.

[12] M. N. Ali, M. Soliman, K. Mahmoud, J. M. Guerrero, M. Lehtonen, and M. M. F. Darwish, "Resilient design of robust multi-objectives PID controllers for automatic voltage regulators: D-decomposition approach," *IEEE Access*, vol. 9, pp. 106589–106605, 2021.

[13] H. Abubakr, J. C. Vasquez, K. Mahmoud, M. M. F. Darwish, and J. M. Guerrero, "Robust PID-PSS design for stability improvement of grid-tied hydro turbine generator," in *Proceedings of the 2021 22nd International Middle East Power Systems Conference (MEPCON)*, pp. 607–612, Assiut, Egypt, December 2021.

[14] W. Jianhua, L. Yaqiong, Z. Haixin, J. Guo, and Z. Xinglong, "Variable Structure Control of buck converter based on inverse system," in *Proceedings of the 3rd International Workshop on Advanced Computational Intelligence*, pp. 609–611, Suzhou, Jiangsu, August 2010.

[15] U. C. de Moura, F. Da Ros, A. M. R. Brusin, A. Carena, and D. Zibar, "Experimental characterization of Raman amplifier optimization through inverse system design," *Journal of Lightwave Technology*, vol. 39, no. 4, pp. 1162–1170, 2021.

[16] L. Yixiao, L. Yinong, Y. Yinghong, and Z. Ling, "Decoupling control of longitudinal and lateral motion for intelligent vehicle based on neural network inverse method," *Journal of Hunan University Natural Sciences*, vol. 46, no. 10, pp. 150–158, 2019.

[17] X. Sun, B. Su, L. Chen, Z. Yang, X. Xu, and Z. Shi, "Precise control of a four degree-of-freedom permanent magnet biased active magnetic bearing system in a magnetically suspended direct-driven spindle using neural network inverse scheme," *Mechanical Systems and Signal Processing*, vol. 88, pp. 36–48, 2017.

[18] Z. Zhang, W. Hongru, Z. Yang, and W. Feng, "Enhanced wind turbine maximum wind-energy capture based on the inverse-system method," *Energy Reports*, vol. 8, no. 4, pp. 475–487, 2022.

[19] L. V. Rueden, S. Mayer, K. Beckh et al., "Informed machine learning-a taxonomy and survey of integrating prior knowledge into learning systems," *IEEE Transactions on Knowledge and Data Engineering*, p. 1, 2021.

[20] G. Liu, R. Chen, D. Zhang, and H. Zhou, "Model-free adaptive robust control for two motor drive system based on neural network inversion," *Proceedings of the CSEE*, vol. 39, no. 3, pp. 868–874, 2019.

[21] M. N. Ali, K. Mahmoud, M. Lehtonen, and M. M. F. Darwish, "Promising MPPT methods combining metaheuristic, fuzzy-logic and ANN techniques for grid-connected photovoltaic," *Sensors*, vol. 21, no. 4, p. 1244, 2021.

[22] M. Elsisi, M. Q. Tran, K. Mahmoud, L. Matti, and M. M. F. Darwish, "Robust design of ANFIS-based blade pitch controller for wind energy conversion systems against wind speed fluctuations," *IEEE Access*, vol. 9, pp. 37894–37904, 2021.

[23] M. Xu, X. Diao, D. Feng, and H. Zhu, "The neural network inverse decoupling control of bearingless synchronous reluctance motor," in *Proceedings of the 32nd Chinese Control Conference*, pp. 3259–3263, Xi'an, China, July 2013.

[24] L. Qu, G. Liu, H. Zhang, and Y. Jiang, "Decoupling control for five-phase fault-tolerant permanent-magnet motor by using SVM inverse system method," in *Proceedings of the 2014 International Joint Conference on Neural Networks (IJCNN)*, pp. 3837–3840, Beijing, China, July 2014.

[25] W. Bu and Z. Li, "LS-SVM inverse system decoupling control strategy of a bearingless induction motor considering stator current dynamics," *IEEE Access*, vol. 7, pp. 132130–132139, 2019.

[26] Z. Cheng, S. Zhang, and Z. Zhang, "Predictive control for coke oven blowing cooler system based on SVR," in *Proceedings of the 2019 Chinese Control And Decision Conference (CCDC)*, pp. 3883–3888, Nanchang, China, June 2019.

[27] U. Kemal and G. G. Öke, "An adaptive state feedback controller based on SVR for nonlinear systems," in *Proceedings of the 2018 6th International Conference on Control Engineering & Information Technology (CEIT)*, pp. 1–5, Istanbul, Turkey, October 2018.

[28] D. Wu and S. Wang, "Comparison of road traffic accident prediction effects based on SVR and BP neural network," in *Proceedings of the 2020 IEEE International Conference on Information Technology,Big Data and Artificial Intelligence (ICIBA)*, vol. 1, pp. 1150–1154, Chongqing, China, November 2020.

[29] "Google Maps," 2021, https://www.google.com/maps/.

[30] A. Serban, L. S. Paraschiv, and S. Paraschiv, "Assessment of wind energy potential based on Weibull and Rayleigh distribution models," *Energy Reports*, vol. 6, pp. 250–267, 2020.